Journal of Vacuum Science and Technology B

RESEARCH ARTICLE | OCTOBER 06 2023

Characterization of porosity in periodic 3D nanostructures using spectroscopic scatterometry

Special Collection: Papers from the 66th International Conference on Electron, Ion and Photon Beam Technology and Nanofabrication (EIPBN 2023)

Kwon Sang Lee ; Kun-Chieh Chien ; Barbara Groh ; I-Te Chen ; Michael Cullinan ; Chih-Hao Chang

J. Vac. Sci. Technol. B 41, 064001 (2023)
https://doi.org/10.1116/6.0003035

JVST B
Journal of Vacuum Science & Technology B
ARTICLE
pubs.aip.org/avs/jvb

Characterization of porosity in periodic 3D nanostructures using spectroscopic scatterometry

Cite as: J. Vac. Sci. Technol. B **41**, 064001 (2023); doi: 10.1116/6.0003035
Submitted: 1 August 2023 · Accepted: 12 September 2023 ·
Published Online: 6 October 2023

Kwon Sang Lee, Kun-Chieh Chien, Barbara Groh, I-Te Chen, Michael Cullinan, and Chih-Hao Chang[a)]

AFFILIATIONS

Walker Department of Mechanical Engineering, The University of Texas at Austin, Austin, Texas 78712

Note: This paper is part of the Special Topic Collection: Papers from the 66th International Conference on Electron, Ion and Photon Beam Technology and Nanofabrication (EIPBN 2023).

[a)]**Author to whom correspondence should be addressed:** chichang@utexas.edu

ABSTRACT

Periodic nanostructures have important applications in nanophotonics and nanostructured materials as they provide various properties that are advantageous compared to conventional solid materials. However, there is a lack of metrology techniques that are suitable for large-scale manufacturing, as the traditional tools used in nanotechnology have limited throughput and depth resolution. In this work, we use spectroscopic scatterometry as a fast and low-cost alternative to characterize the porosity of three-dimensional (3D) periodic nanostructures. In this technique, the broadband reflectance of the structure is measured and fitted with physical models to predict the structure porosity. The process is demonstrated using 3D periodic nanostructures fabricated using colloidal phase lithography at various exposure dosages. The measured reflectance data are compared with an optical model based on finite-difference time-domain and transfer-matrix methods, which show qualitative agreement with the structure porosity. We found that this technique has the potential to further develop into an effective method to effectively predict the porosity of 3D nanostructures and can lead to real-time process control in roll-to-roll nanomanufacturing.

I. INTRODUCTION

Periodic 3D nanostructures, defined by their nanoscale features and periodicity in three dimensions, have become increasingly important in emerging research. Initial interest in such structures emerged in the 1980s from their applications in photonic crystals, which can create a photonic energy bandgap where no propagation modes can exist.[1–4] Periodic 3D nanostructures do have attractive properties not only for uses as photonic crystals but also for other nanophotonic applications. In nature, there exists a large gap between the refractive indexes of solid materials and air, with the lowest conventional material being MgF_2. Although aerogel and other nanoporous materials have bridged the gap between conventional materials in terms of optical indices, such materials are randomly porous and have poor mechanical properties. Recent work has demonstrated 3D nanolattice structures with indices as low as 1.025 and that are mechanically robust enough to be integrated into multilayer films.[5,6] Aerogels have also been shown to have low thermal conductivity; however, they comparatively lack mechanical stiffness compared to their periodic counterparts.[7,8] Recent work has shown periodic 3D nanostructures to have comparably low thermal conductivity while maintaining high stiffness.[9] Another application that is increasing in relevance is battery technology, where 3D nanostructures are used to create ultrafast charging and discharging battery electrodes.[10]

One common method for metrology of nanostructures is scanning electron microscopy (SEM), which detects the secondary or backscattered electrons from the beam-sample interaction and can have nanoscale resolution.[11,12] Although SEM is well established within the scientific community, this technique is inadequate for *in situ* large-scale 3D measurements for large-scale manufacturing due to some drawbacks. First, it has low throughput and is slow when used for large-scale metrology over the entire substrate.[13] Second, SEM is a destructive technique and requires cross-sectioning of 3D samples to acquire data in depth as it can only capture 2D data from the surface. Third, electron interactions are material-dependent, and, typically, a conductive layer needs to be coated for nonconductive materials to prevent charging, which might be undesirable depending on applications.[11] Similarly, transmission electron microscopy (TEM) analyzes transmitted, diffracted, or scattered electrons, depending on the mode, through a

thin sample to obtain the critical dimensions. Although it provides atomic scale resolution, TEM can only measure thin samples, typically up to 100 nm, to ensure a sufficient electron signal. In addition, TEM is time consuming as scanning speeds are low and costly.[11] Atomic force microscopy and other probe-based microscopy techniques detect the response of a microscale cantilever to measure the topography and some material properties such as the material's Young's modulus.[12,14,15] More recently, researchers have applied it in the roll-to-roll (R2R) manufacturing of flexible substrates[16] and have developed integrated metrology systems to increase throughput.[17] However, such profilometry techniques are generally limited to surface measurements and do not provide volumetric information for 3D nanostructures.

Optical techniques can also be employed for nanoscale metrology, which uses the scattering of light across a large area to measure the structure features. Critical dimension small angle x-ray scattering is one such method, where the scattering pattern for a modeled shape function is compared to the measured scattering data.[13,18,19] However, this method requires x-ray sources with high photon flux that are not readily available.[20] Optical scatterometry is another well-established method, which has been used since the 1940s to measure optical constants of materials[21,22] and has been applied to dimensional metrology.[23–27] Spectroscopy uses the reflectance spectra of the structure versus either incident angles, known as angular spectroscopy, or wavelengths, known as spectroscopy scatterometry. More recently, an in-line metrology angular spectroscopy method for R2R has been developed for the metrology of 20 nm pitch wire grid polarizers using a 405 nm light source.[28] Recent studies have also demonstrated hyperspectral imaging for the high-throughput characterization of large-area 2D nanostructure arrays.[29] While there has been extensive work in the metrology of 2D/2.5D nanostructures using scatterometry, their applications in 3D nanostructures have been less explored.

In this work, we present a computational framework based on spectroscopic scatterometry to characterize the porosity of periodic 3D nanostructures. This approach is based on building an optical model of the 3D nanostructures using effective medium theory and comparing the predicted reflectance with the measured spectra. To validate the model, experimental reflectance spectra are obtained from 3D nanostructures fabricated using self-assembled colloidal phase lithography. The optical model constructed is based on the finite-difference time-domain (FDTD) method to simulate the volumetric intensity profile, which can be used to predict the 3D geometry in the photoresist using a binary resist model. The critical dimension of the fabricated structures is then used to empirically calibrate for the threshold dose and predict the nanostructure porosity. The reflectance spectra from the 3D nanostructures are then modeled using the transfer-matrix method (TMM) and compared with the measured reflectance. This approach takes advantage of scatterometry's high throughput and versatility, and it can lead to real-time exposure control of 3D nanostructures in roll-to-roll nanomanufacturing.

II. EXPERIMENTAL METHODS

A. Fabrication process

Fabrication of the 3D nanostructure samples is based on colloidal phase lithography reported previously and is illustrated in Fig. 1.[30–33] In this work, 350 nm polystyrene nanospheres (PolySciences) suspended in aqueous solution are used for the self-assembly process, which was performed using the Langmuir–Blodgett method in a glass beaker. The film can then be transferred to a silicon wafer coated with an antireflection coating (ARC-Icon, Brewer) and positive photoresist (PFI-88A2, Sumitomo Chemical). The samples were exposed to HeCd laser (325 nm wavelength, Kimmon) at normal incident in varying dosages from 70 to 110 mJ/cm^2, as shown in Fig. 1(a). After removing the nanospheres in an ultrasonic bath, the samples are then developed in a developer (CD-26 Developer, Microposit), resulting in 3D nanostructures in the photoresist as shown in Fig. 1(b). A halogen light source (DH-2000-BAL, Ocean Insight) directed by an optical cable and a spectrometer (range of 190–1100 nm, HR4Pro, Ocean Insight) is used to measure the reflectance spectra from the fabricated samples, as illustrated in Fig. 1(c).

B. Simulation and modeling

The theoretical modeling mimics the experimental process as depicted in Fig. 1, where each stage of the experimental process, namely, lithography, 3D nanostructure structure, and reflectance measurement, has an equivalent model. The lithography modeling is performed using FDTD (Ref. 34) methods (Lumerical, Ansys), as shown in Fig. 1(d). Here, the Si substrate, ARC, photoresist, and the colloidal array are illuminated with a narrowband 325 nm wavelength light, and the Poynting vector of each unit cell within the photoresist was used to calculate the effective power based on the Poynting theorem.[35,36] Based on the relative dosages each cell has received, a binary model is used to emulate the photochemical response of a positive photoresist, where any volume receiving intensity above the threshold dose dissolves, as shown in Fig. 1(e). The binary resist model can serve as a reference to empirically calculate porosity by comparing the simulated diameters with those measured experimentally from the top-view SEMs of the fabricated structures.

An effective medium theory model is used to approximate the nanostructure as a homogeneous film and to simulate the reflectance based on TMM,[37] as shown in Fig. 1(f). This approach is taken since the parameter of interest in this work is the volume fraction of air or porosity, which has a direct influence over the nanostructure effective index. The model is based on a layer stack containing semi-infinite air, the nanostructure simulated as a homogenous layer, the ARC layer, and the Si substrate modeled as a semi-infinite medium. We used experimentally obtained values for the optical refractive indices, n, and absorption, k, for the photoresist. The values for ARC are from the manufacturer and are from the literature for Si.[38] The effective index n_{eff} and absorption k_{eff} of the nanostructure layer can be modeled based on an effective medium theory using the volume averaging theorem model,[39] given as

$$n_{\text{eff}}^2 = \frac{1}{2}\left[A + \sqrt{A^2 + B^2}\right], \tag{1}$$

$$k_{\text{eff}}^2 = \frac{1}{2}\left[-A + \sqrt{A^2 + B^2}\right], \tag{2}$$

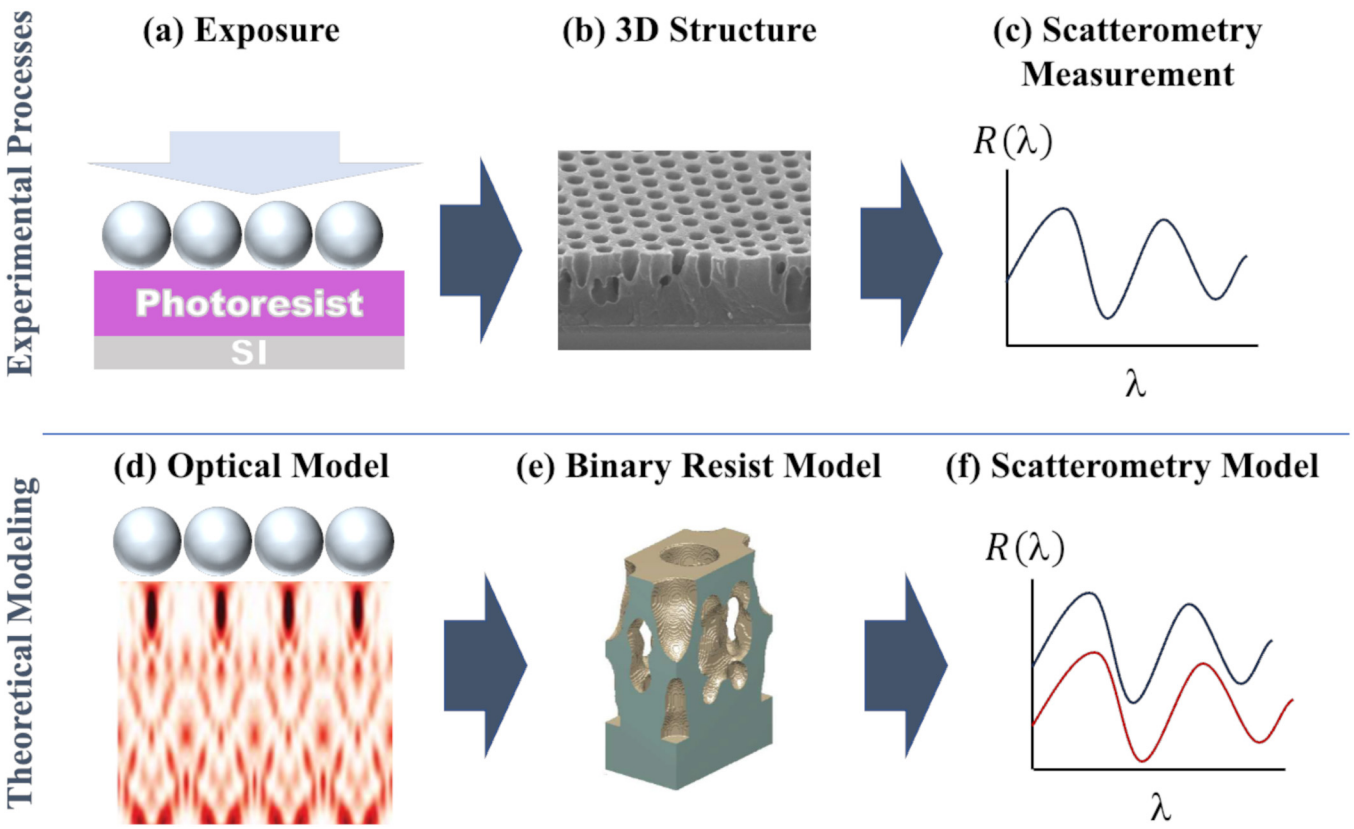

FIG. 1. Schematic of a computational and experimental framework for the metrology of porosity in 3D nanostructures. (a) Nanosphere interference lithography, (b) photoresist after development, (c) measurement of reflectance using a spectrometer, (d) optical model of the lithography process, (e) binary resist model, and (f) scatterometry model.

$$A = \phi(n_a^2 - k_p^2) + (1-\phi)(n_a^2 - k_p^2), \tag{3}$$

$$B = 2n_a k_a \phi + 2n_p k_p (1-\phi), \tag{4}$$

where ϕ is the porosity or the volume ratio of the photoresist, n_a and n_p are the refractive indices of air and the photoresist, respectively, and k_a and k_p are the absorption index of air and the photoresist, respectively. The reflectance at the normal incident angle for the different porosity is then calculated for the 400–1000 nm wavelength range to match the experiments.

III. RESULTS AND DISCUSSION

A. Fabrication results

The fabricated 3D nanostructures in the photoresist are depicted in Fig. 2. Here, the samples exposed to 70, 90, and 110 mJ/cm^2 are illustrated in the top-view SEM images, as shown in Figs. 2(a)–2(c), respectively. The corresponding cross-sectional SEM images are shown in Figs. 2(d)–2(f), and the 3D nature of the structure can be observed. It can be noted that the 70 mJ/cm^2 samples are underexposed, and the exposure dose was too low for light to fully expose the bottom of the photoresist layer, as shown in Figs. 2(a) and 2(d). The 90 mJ/cm^2 samples are adequately exposed, resulting in the desired 3D nanostructures as shown in Figs. 2(b) and 2(e). The 110 mJ/cm^2 sample has the highest porosity and is slightly overexposed, as some sagging of the top layer in the structure is observed, as shown in Figs. 2(c) and 2(f).

The average, minimum, and maximum diameters of the holes and their standard deviations for all the samples are measured and tabulated in Table I. Here, it can be observed that the hole diameter increases with the exposure dose, as expected for a positive photoresist. In all three cases, defects and particle size distribution from the nanosphere self-assembly created slight variations in the structures. The variations in the nanosphere mask result in nonuniformity of the intensity distribution, which can result in varying diameter sizes of ~10 nm in the patterned structures. The measured hole diameter is then used with the optical lithography model, as described in Sec. III B, to calibrate the porosity of the fabricated structures.

The experimental reflectance measurements from the fabricated samples are shown in Fig. 3. Here, the absolute reflectance is

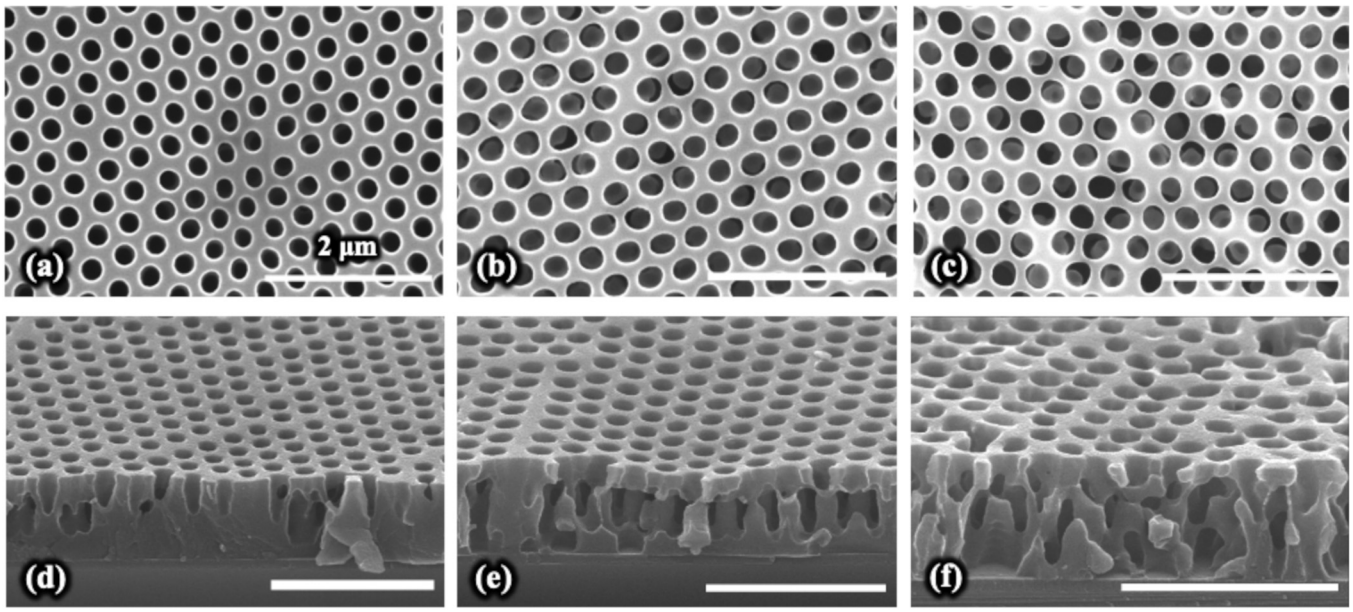

FIG. 2. Fabrication results of the patterned 3D nanostructures at various exposure doses. Top-view SEM images of (a) 70, (b) 90, and (c) 110 mJ/cm^2 samples. Cross-sectional SEM images of (d) 70, (e) 90, and (f) 110 mJ/cm^2 samples. All scale bars represent 2 μm.

measured from the specular reflection order. The general pattern is that the reflected intensity for all samples is modulated due to interference effects, and the reflectance increases as the wavelength increases. However, all three reflectance spectra show different modulation periods and amplitudes, as well as different intensity peaks and valleys. These differences could be attributed to the larger porosities in the 90 and 110 mJ/cm^2 dosage samples and will be used for reflectance modeling to predict porosity.

B. Simulation results

The simulated intensity profile of the colloidal phase lithography process is shown in Fig. 4. The normalized 2D intensity maps in *y-z* and *x-z* planes at the center of the unit cell are shown in Figs. 4(a) and 4(b), respectively. Here, it can be observed that the light forms an intensity peak right under the nanospheres, thereby creating the holes shown in Fig. 2. The intensity peak is repeated in the z direction after 707 nm, which can be calculated as the Talbot distance where the primary intensity pattern is repeated. The simulated 3D intensity pattern and its corresponding predicted structure in the photoresist are shown in Figs. 4(c) and 4(d), respectively. Here, the photochemical response of the photoresist is modeled with a binary resist model, where any value above the dose threshold has been removed from the volume. The simulated structure has a porosity of 45% with the diameter of the top layer

TABLE I. Measured diameters of the holes in the top layers of the samples using SEM.

Exposure (mJ/cm^2)	Average (nm)	Std. dev. (nm)	Min (nm)	Max (nm)
70	229	10	197	247
90	242	9	222	275
110	253	11	226	293

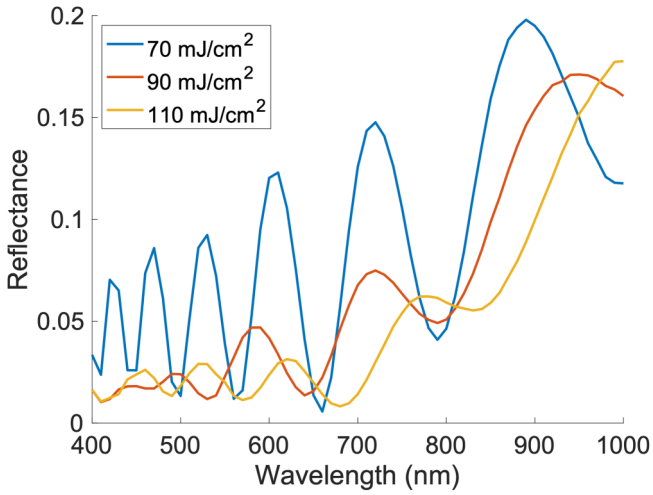

FIG. 3. Reflectance measurements of fabricated samples with 70, 90, and 110 mJ/cm^2 exposure doses vs wavelength.

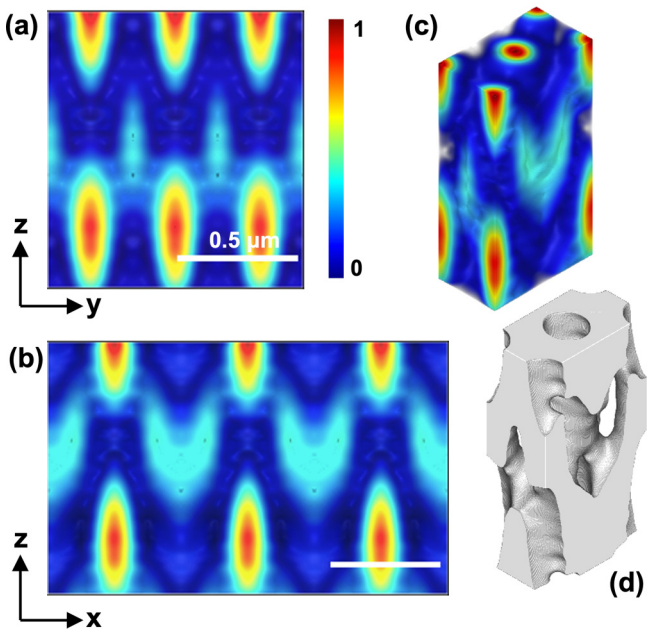

FIG. 4. Simulated intensity profiles from the optical FDTD model. Two-dimensional intensity profile across (a) *y-z* plane and (b) *x-z* plane through the center of the unit cell. (c) Simulated 3D intensity profile and corresponding (d) simulated photoresist structure using the binary resist model with 45% porosity.

being approximately 230nm, which is equivalent to that of the 70 mJ/cm^2 dosage sample. The simulated photoresist geometry shows qualitative agreement with the structures obtained from the experimental 70 mJ/cm^2 sample, as shown in Fig. 2(a), albeit without some of the defects present in the fabricated structure.

Table II tabulates the porosity estimates from the FDTD simulations based on the diameter of the holes between 20% and 80% in increments of 10% and the average diameters of each dosage from Table I. Using this optical model, the diameter of the top layer from the SEM images can be used to fit the threshold value to empirically calculate the structure porosity. Table II is also interesting as the diameter and the porosity do not have a linear relationship, though generally increasing with each other. In other words, in some ranges of diameters, small diameter changes mean a large porosity change, while in other regions, large diameter changes mean small changes in porosity. This is also evident in the table where between 60% and 70% porosity, the diameter changes by 20 nm, while between 30% and 40% porosity, the diameter changes by 13 nm. This introduces an interesting inverse design problem, and one must design the lithography conditions depending on their needs. For example in the case of porosity control, the system should be designed so that small changes in porosity will lead to large changes in surface diameter. This design would ensure even small porosity changes can be detected so that adjustments can be made. While on the opposite case, if control of the surface diameter is important the porosity variance may be ignored and instead accommodate a larger range of dosages from the lithography step.

TABLE II. FDTD based approximations of the porosity based on surface diameter.

Porosity (%)	Diameter (nm)	Porosity (%)	Diameter (nm)
20	180	60	238
30	195	62	242
40	208	68	253
50	222	70	258
55	229	80	283

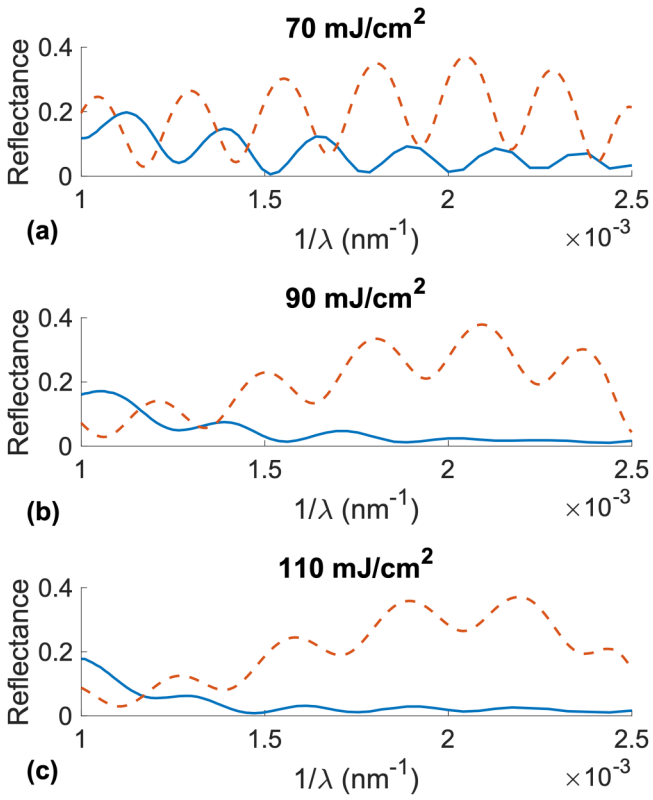

FIG. 5. Comparison of experimentally measured and simulated reflectance for (a) 70, (b) 90, and (c) 110 mJ/cm^2. Due to light scattering defects, the simulated best match is found for oscillation characteristics in the reflectance spectra by matching the period of the intensity oscillations and not the phase and absolute intensity.

Once the nanostructure porosity can be modeled using the calibration data from the SEM images, it can be used to validate the effective medium model. The calculated reflectance using TMM is compared with the measured reflectance data in the spatial frequency domain, as shown in Fig. 5. The frequency domain is examined to reduce the variations in oscillation periods, which is due to material dispersion. It can be noted that the absolute reflectance obtained from experiments is consistently lower than that calculated from the model, which can be attributed to scattering losses

in the fabricated nanostructures due to colloidal assembly defects. This effect is characteristic of self-assembled patterns, which are typically locally periodic but lack long-range spatial-phase coherence. The defects result in more diffused light from scattering and reduce the specular order that is measured. The scattering is also higher at shorter wavelengths, resulting in lower measured reflectance at a higher spatial frequency region, as observed from Fig. 5. Note that there is also a phase offset between the experimental and simulated spectra due to differences in the thicknesses of the layers, which are not fitted for in the model. Therefore, we examine the oscillation characteristics in the reflectance spectra, namely, matching the period of the intensity oscillations. For each case, the closest simulated matching period length is calculated by averaging the peak-to-peak and valley-to-valley distances from the TMM, which are also plotted as a dashed line. For all cases, the best matching period length has a very low error of <2%.

The average oscillation period of the reflectance spectra in the spatial frequency domain from the TMM as a function of predicted porosity is shown in Fig. 6. A five-point moving average is used to reduce noise and smoothen the simulated periods. The solid circles represent the porosity calculation based on the experimental data for the 70, 90, and 110 mJ/cm^2 dose samples, which agrees well with the overall trend. The horizontal error bars indicate the porosity error calculated using the standard deviation from the observed variation in diameters of the holes of the top layer using SEM. The vertical error bars represent the standard deviation of the period length observed in the measured spectra, which is due to material dispersion in the photoresist layer. In the TMM model, the porosity increases with the average oscillation period, but the relationship is not directly proportional. The experimental porosity empirically fitted from the fabricated structures also confirms this relationship. Comparing each data point, the 70 mJ/cm^2 sample has an empirical porosity of 55% with an average period length of 2.43×10^{-4} nm, which would correspond to 25% in the TMM model. The disagreement here can be attributed to underexposure, which results in a full solid layer at the bottom of the photoresist. Therefore, the air pores in the model are assumed to be uniformly distributed within the whole layer, while they are confined to only the top portion of the fabricated structures. A more accurate model is to include the 3D exposure of the photoresist into consideration, which is the subject of ongoing work. At higher doses, the 90 and 110 mJ/cm^2 samples have better agreement. The empirically fitted porosities for the 90 and 110 mJ/cm^2 samples are 38% and 32% and agree well with the TMM model of 37% and 26%, corresponding to period lengths of 2.928×10^{-4} and 3.037×10^{-4} nm, respectively. Although there is some disagreement for the 70 mJ/cm^2 due to underexposure, there is qualitative agreement in the porosity trends between the experimental results and the simulated results.

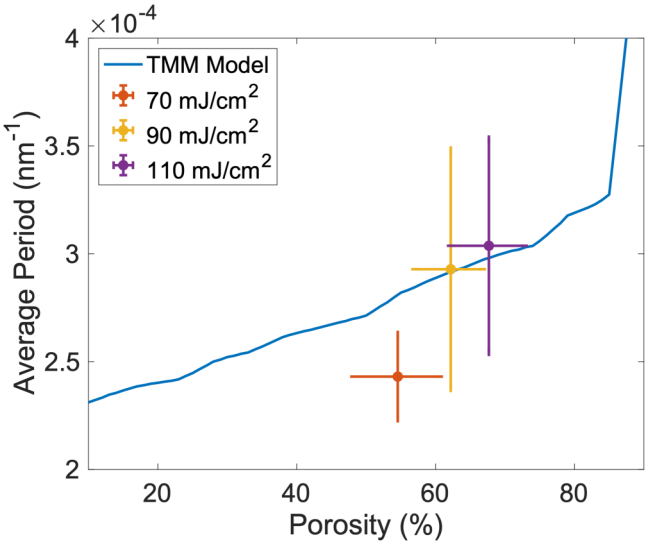

FIG. 6. Average oscillation period in the spatial frequency domain vs predicted porosity of simulated and measured reflectance in the spatial frequency domain.

One major limitation of this method is the need for prior knowledge of the intensity pattern from the lithographic process. If given a random sample, the process would not be able to characterize the features of the sample using this method. However, because the objective of the proposed method is to be able to characterize 3D nanostructure *in situ* in a manufacturing environment, the users can calculate the intensity pattern using the lithography mask pattern and any related material properties. Another limitation is the differences in the measured absolute reflectance and the simulated spectra. This discrepancy can be attributed to scattering losses due to the self-assembled colloidal films, as such methods are prone to assembly defects as observed in Fig. 2. This error can be mitigated by using methods that yield higher defect-free areas or using larger area phase masks molded from defect-free templates. Another limitation is the homogenous film approximation when simulating the reflectance spectra, which is computationally more efficient since the TMM is much faster compared to techniques such as FDTD. However, by substituting the complex 3D structure with a homogenous film, scattering effects within the 3D structure of the film have been ignored, leading to differences in reflectivity. Therefore, future work will focus on more rigorous methods such as FDTD to simulate the reflectivity spectra of the 3D nanostructure. This approach will also allow the prediction of the structure geometry in addition to the porosity studied in this work.

IV. SUMMARY AND CONCLUSIONS

We have demonstrated the use of spectroscopic scatterometry in the measurement of porosity in a 3D nanostructure. We fabricated a 3D nanostructure using colloidal phase lithography and measured the diameters of the holes formed on the top surface. The diameter data are then compared to those of binary models obtained from FDTD simulations to empirically calculate the expected structure porosity. The reflectance spectra of the fabricated samples were measured and compared with those simulated using the TMM, which resulted in qualitative agreement. The experimental data and validated model demonstrate the potential of this method to determine the nanostructure porosity by comparing the periods of the oscillation behavior with further research and larger sample sizes. The concept expands spectroscopic scatterometry from its traditional 2D/2.5D structure characterization,

providing a fast, inexpensive, *in situ* metrology method for periodic 3D nanostructures.

ACKNOWLEDGMENTS

This work was performed at UT Austin Texas Materials Institute (TMI), the Nanomanufacturing System for Mobile Computing and Energy Technologies (NASCENT), and Texas Nanofabrication Facilities, which was supported by the National Science Foundation (NSF) as part of the National Nanotechnology Coordinated Infrastructure (NNCI) under Grant No. NNCI-2025227. This work was funded by NSF (Award No. CMMI:2229036).

AUTHOR DECLARATIONS

Conflict of Interest

The authors have no conflicts to disclose.

Author Contributions

Kwon Sang Lee: Data curation (equal); Investigation (equal); Visualization (equal); Writing – original draft (lead); Writing – review & editing (equal). **Kun-Chieh Chien:** Data curation (equal); Investigation (equal); Methodology (equal); Visualization (equal). **Barbara Groh:** Writing – review & editing (supporting). **I-Te Chen:** Investigation (equal). **Michael Cullinan:** Funding acquisition (lead); Supervision (supporting); Writing – review & editing (equal). **Chih-Hao Chang:** Conceptualization (lead); Data curation (lead); Formal analysis (lead); Funding acquisition (equal); Investigation (lead); Methodology (lead); Project administration (lead); Resources (lead); Software (equal); Supervision (lead); Validation (lead); Visualization (equal); Writing – original draft (equal); Writing – review & editing (lead).

DATA AVAILABILITY

The data that support the findings of this study are available within the article.

REFERENCES

[1]S. John, Phys. Rev. Lett. **58**, 2486 (1987).
[2]E. Yablonovitch and T. J. Gmitter, Phys. Rev. Lett. **63**, 1950 (1989).
[3]M. Qi, E. Lidorikis, P. T. Rakich, S. G. Johnson, J. D. Joannopoulos, E. P. Ippen, and H. I. Smith, Nature **429**, 538 (2004).
[4]E. Yablonovitch, Phys. Rev. Lett. **58**, 2059 (1987).
[5]X. A. Zhang, A. Bagal, E. C. Dandley, J. Zhao, C. J. Oldham, B.-I. Wu, G. N. Parsons, and C.-H. Chang, Adv. Funct. Mater. **25**, 6644 (2015).
[6]I. Chen, Z. Dai, D. T. Lee, Y. Chen, G. N. Parsons, and C. Chang, Adv. Mater. Interfaces **8**, 2100690 (2021).
[7]T. A. Schaedler, A. J. Jacobsen, A. Torrents, A. E. Sorensen, J. Lian, J. R. Greer, L. Valdevit, and W. B. Carter, Science **334**, 962, (2011).
[8]X. Zheng *et al.*, Science **344**, 1373, (2014).
[9]N. G. Dou, R. A. Jagt, C. M. Portela, J. R. Greer, and A. J. Minnich, Nano Lett. **18**, 4755 (2018).
[10]H. Zhang, X. Yu, and P. V. Braun, Nat. Nanotechnol. **6**, 277 (2011).
[11]A. C. Diebold, *Handbook of Silicon Semiconductor Metrology* (Marcel Dekker, Inc., New York, 2001).
[12]N. G. Orji *et al.*, Nat. Electron. **1**, 532 (2018).
[13]Z. Ma and D. G. Seiler, *Metrology and Diagnostic Techniques for Nanoelectronics* (Jenny Stanford, Singapore, 2017).
[14]G. Binnig, C. F. Quate, and Ch. Gerber, Phys. Rev. Lett. **56**, 930 (1986).
[15]R. Dixson and N. G. Orji, Proc. SPIE **6518**, 651816 (2007).
[16]L. G. Connolly, T.-F. Yao, A. Chang, and M. Cullinan, Precis. Eng. **57**, 137 (2019).
[17]T.-F. Yao, L. G. Connolly, and M. Cullinan, J. Micro/Nanolithogr., MEMS, MOEMS **18**, 1 (2019).
[18]A. C. Diebold, J. Vac. Sci. Technol. A **31**, 050804 (2013).
[19]I. W. Hamley, *Small-Angle Scattering: Theory, Instrumentation, Data and Applications*, 1st ed. (Wiley, Hoboken, NJ, 2021).
[20]R. J. Kline, D. F. Sunday, D. Windover, and B. D. Bunday, J. Micro/Nanolithogr., MEMS, MOEMS **16**, 014001 (2017).
[21]J. R. Collins and R. O. Bock, Rev. Sci. Instrum. **14**, 135 (1943).
[22]R. O. Bock, Phys. Rev. **68**, 210 (1945).
[23]R. Zhu, S. R. J. Brueck, N. Dawson, T. Busani, P. Joseph, S. Singhal, and S. V. Sreenivasan, J. Vac. Sci. Technol. B **34**, 06K503 (2016).
[24]A. C. Diebold, A. Antonelli, and N. Keller, APL Mater. **6**, 058201 (2018).
[25]B. M. Barnes, M. Y. Sohn, F. Goasmat, H. Zhou, A. E. Vladár, R. M. Silver, and A. Arceo, Opt. Express **21**, 26219 (2013).
[26]B. M. Barnes, R. Attota, R. Quintanilha, Y.-J. Sohn, and R. M. Silver, Meas. Sci. Technol. **22**, 024003 (2011).
[27]R. M. Silver, B. M. Barnes, R. Attota, J. Jun, M. Stocker, E. Marx, and H. J. Patrick, Appl. Opt. **46**, 4248 (2007).
[28]R. Zhu, J. J. Faria-Briceno, S. R. J. Brueck, P. Joseph, S. Singhal, and S. V. Sreenivasan, AIP Adv. **10**, 015140 (2020).
[29]B. Gawlik, C. Barrera, E. T. Yu, and S. V. Sreenivasan, Opt. Express **28**, 14209 (2020).
[30]I.-T. Chen, E. Schappell, X. Zhang, and C.-H. Chang, Microsyst. Nanoeng. **6**, 22 (2020).
[31]V. A. Premnath, I.-T. Chen, K.-C. Chien, and C.-H. Chang, J. Vac. Sci. Technol. B **40**, 062803 (2022).
[32]X. A. Zhang, I.-T. Chen, and C.-H. Chang, Nanotechnology **30**, 352002 (2019).
[33]C.-H. Chang, L. Tian, W. R. Hesse, H. Gao, H. J. Choi, J.-G. Kim, M. Siddiqui, and G. Barbastathis, Nano Lett. **11**, 2533 (2011).
[34]Kane Yee, IEEE Trans. Antennas Propag. **14**, 302 (1966).
[35]J. H. Poynting, Philos. Trans. R. Soc. Lond. **175**, 343 (1884).
[36]D. J. Griffiths, *Introduction to Electrodynamics*, 4th ed. (Pearson, Boston, 2013).
[37]A. Yariv and P. Yeh, *Optical Waves in Crystals: Propagation and Control of Laser Radiation*, Wiley classics library ed. (Wiley, Hoboken, NJ, 2003).
[38]E. D. Palik and G. Ghosh, *Handbook of Optical Constants of Solids* (Academic, San Diego, 1998).
[39]A. Garahan, L. Pilon, J. Yin, and I. Saxena, J. Appl. Phys. **101**, 014320 (2007).